

## LETTERS

# The dynamics of melt and shear localization in partially molten aggregates

Richard F. Katz<sup>1</sup>, Marc Spiegelman<sup>1,2</sup> & Benjamin Holtzman<sup>1</sup>

The volcanoes that lie along the Earth's tectonic boundaries are fed by melt generated in the mantle. How this melt is extracted and focused to the volcanoes, however, remains an unresolved question. Here we present new theoretical results with implications for melt focusing beneath mid-ocean ridges. By modelling laboratory experiments<sup>1,2</sup>, we test a formulation for magma dynamics and provide an explanation for localized bands of high-porosity and concentrated shear deformation observed in experiments. These bands emerge and persist at 15°–25° to the plane of shear. Past theoretical work on this system predicted the emergence of melt bands<sup>3,4</sup> but at an angle inconsistent with experiments. Our results suggest that the observed band angle results from a balance of porosity-weakening and strain-rate-weakening deformation mechanisms. Lower band angles are predicted for greater strain-rate weakening. From these lower band angles, we estimate the orientation of melt bands beneath mid-ocean ridges and show that they may enhance magma focusing toward the ridge axis.

Recent experiments<sup>1,2</sup> demonstrate that partially molten aggregates deformed in simple shear develop localized melt bands of high porosity and enhanced strain (Fig. 1a). These bands emerge at low angles (~20°) to the plane of shear for a range of strain rates and stresses, and persist at low angles even after large shear strains. This pattern-forming instability presents a rare opportunity to test theories of magma transport in the Earth's mantle<sup>5–8</sup>. Magma dynamics theories use continuum equations for conservation of mass, momentum and energy to describe a two-phase system of low-viscosity magma in a deformable, permeable solid matrix and should be applicable to the experiments. Past theoretical work<sup>3</sup> showed that a porosity-weakening viscous material<sup>9</sup> undergoing extension is unstable: tension across a weak, high-porosity region leads to low pressure that, in turn, causes convergence of melt flow into that region, raising its porosity and further weakening it. This instability has been predicted to occur at scales smaller than the compaction length<sup>3,4,10,11</sup>, which is the intrinsic length-scale in magma dynamics theory<sup>5</sup>.

Past theoretical work predicts that melt bands emerge perpendicular to the direction of the maximum rate of extensional strain. This prediction results from assuming that the matrix viscosity depends only on porosity and weakens with increasing melt fraction. For simple shear geometry, Spiegelman<sup>4</sup> showed that bands oriented at 45° to the shear plane will grow fastest, whereas melt bands with angles greater than 90° will decay (Supplementary Fig. S1). Here we demonstrate that a viscosity that includes both porosity and strain-rate-weakening mechanisms can reproduce the emergence and persistence of melt bands at about 20° to the direction of maximum shear (a difference of 25° from past predictions), as observed in experiments.

A power-law form for strain-rate weakening is a commonly

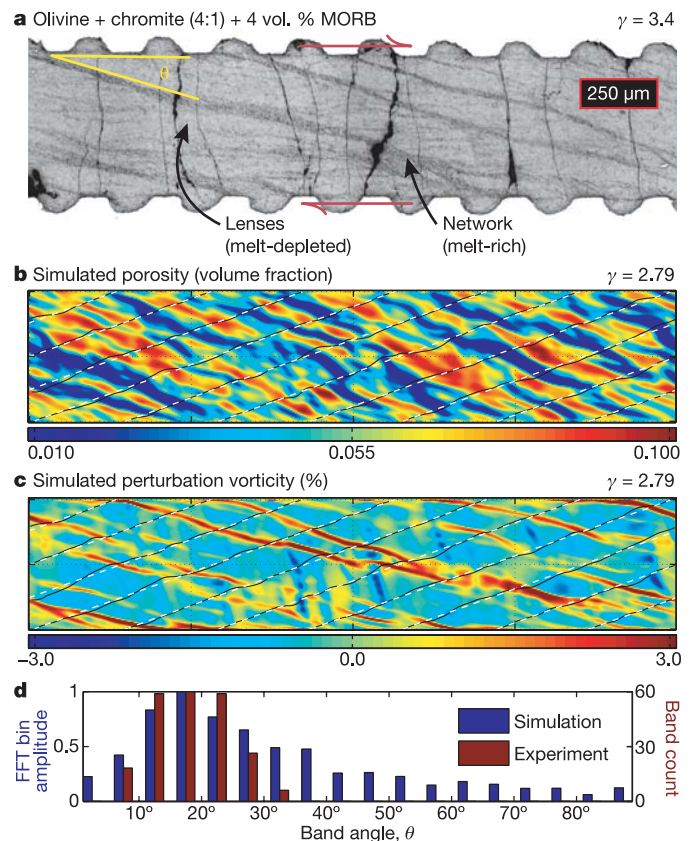


**Figure 1** | **A comparison of experimental and numerical results.** **a**, An example cross-section of an experiment (PI-1096) on a partially molten olivine-basalt-chromite aggregate deformed in simple shear to a strain of 3.4. (Adapted from Fig. 1a of ref. 18; experimental details in ref. 2.) The melt-rich bands are sloping, darker-grey regions at an angle  $\theta$  to the shear plane. Sub-vertical black features are decompression cracks, an experimental artefact. **b**, **c**, The porosity (**b**) and perturbation vorticity (**c**) from a numerical simulation with  $n = 6$  and  $\alpha = -27$  at a shear strain  $\gamma$  of 2.79. The domain is five by one compaction lengths, approximately equal to the estimated size of an experimental charge. The perturbation vorticity,  $\nabla \times [V - \gamma y i] / \dot{\gamma}$ , is the total vorticity minus the constant vorticity  $\dot{\gamma}$  due to simple shear (here normalized by  $\dot{\gamma}$ ). Black lines in **b** and **c** show the position of passive tracer particles that were arrayed in vertical lines at  $\gamma = 0$ ; white dotted lines show the expected position of the tracers due only to simple shear. The linear, low-angle red bands in **c** are weak regions associated with high porosity and enhanced shear, while the linear, sub-vertical blue regions are regions of reversed shear. **d**, Histograms comparing band-angle distributions in experiments and the numerical solution from **b**.

<sup>1</sup>Lamont-Doherty Earth Observatory of Columbia University, Palisades, New York 10964, USA. <sup>2</sup>Department of Applied Physics and Applied Mathematics, Columbia University, New York, New York 10027, USA.

accepted constitutive relation for high-temperature creep of mantle materials<sup>9,12</sup>. Here we assume<sup>9,12–14</sup>:

$$\eta(\phi, \dot{\epsilon}) = \eta_0 e^{\alpha(\phi - \phi_0)} \dot{\epsilon}_{II}^{\frac{1-n}{n}} \quad (1)$$

where  $\eta_0$  is the shear viscosity at the reference porosity  $\phi_0$  and reference strain rate.  $\alpha = -28 \pm 3$  is an experimentally derived porosity-weakening coefficient<sup>14,15</sup>,  $\dot{\epsilon}_{II}$  is the second invariant of the strain-rate tensor, and  $n$  defines the power-law dependence of viscosity on stress. This viscosity is newtonian when  $n = 1$  and is a standard non-newtonian power-law viscosity when  $n > 1$  and  $\phi = 0$ .

To understand the effect of the strain-rate dependence of viscosity we extend a previous linear analysis<sup>4</sup>. Formally, we introduce an infinitesimal plane-wave perturbation (analogous to a melt-rich band) to a constant-porosity system undergoing simple shear and solve for its growth as a function of orientation (Supplementary Information). The growth rate,  $\dot{s}$ , of porosity bands predicted by this analysis is:

$$\dot{s}(\theta, n) = -\frac{\alpha \xi (1 - \phi_0) \sin(2\theta)}{1 + \frac{1-n}{n} \cos^2(2\theta)} \quad (2)$$

where  $\theta(t)$  is the angle between the melt bands and the shear plane (Fig. 1a), which increases with time,  $t$ , due to advection by the shear flow. The parameter  $\xi = (\xi_0/\eta_0 + 4/3)^{-1}$  depends on the ratio of bulk viscosity to shear viscosity and controls the growth rate of band

porosity through the product  $\alpha \xi$ . The amplitude of porosity in the bands at strain  $\gamma(t)$  is given by  $e^{s(t)}$ .

Figure 2a shows the growth rate of melt bands as a function of their angle to the shear plane,  $\theta$ , and the stress exponent,  $n$ . For a viscosity that weakens with porosity only, melt bands oriented at 45° grow fastest because they are perpendicular to the direction of maximum extension in simple shear (equation (2) with  $n = 1$ ).

For a strain-rate-dependent viscosity ( $n > 1$ ), however, concentrated shear deformation further weakens the bands, allowing them to more easily de-compact under extension. Enhanced shear strain is largest for porosity bands oriented at zero and 90° and goes to zero for 45° bands (Supplementary Fig. S1 and  $\cos^2(2\theta)$  term in equation (2)). Thus two competing processes affect the preferred angle of melt bands. The balance between favourable orientation for extension (45°) and favourable orientation for concentrating shear (0 and 90°) is controlled by the factor  $(1 - n)/n$ . Figure 2a shows the effect of changing  $n$  on the growth rate of porosity. As  $n$  increases from 1 to 6, the single peak in  $\dot{s}$  at 45° broadens and divides into symmetric peaks at low (~15°) and high (~75°) angle.

Although the instantaneous growth rate of melt bands in Fig. 2a is symmetric about 45°, advection by simple shear affects low- and high-angle bands differently. Low-angle bands are rotated slowly and persist in favourable orientations for growth of porosity. High-angle bands, however, are rapidly rotated away from angles with positive growth rates. Figure 2b shows that after a strain of  $\gamma = 1$ , bands at low

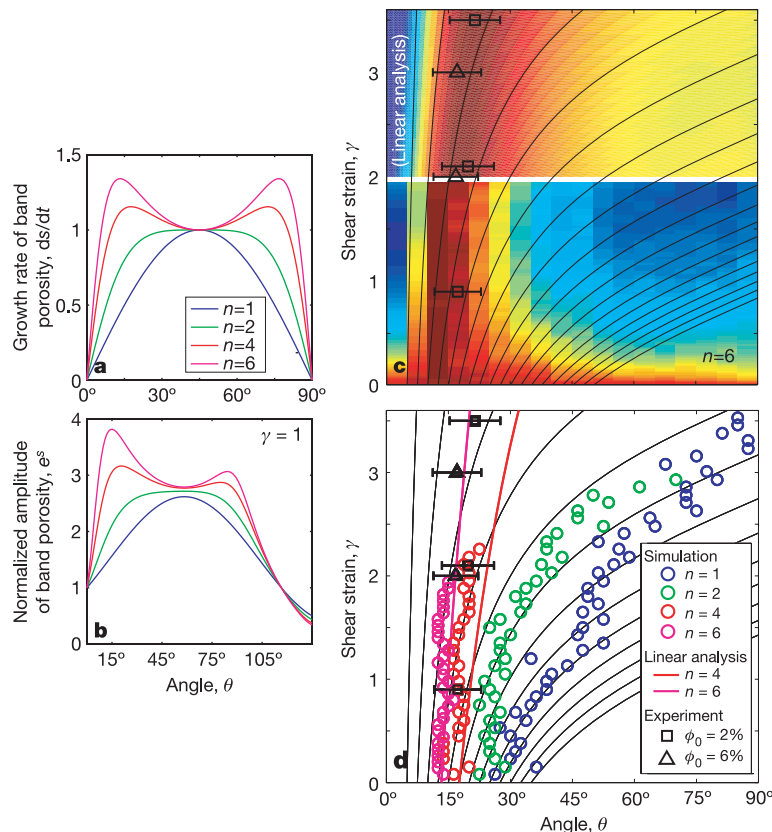


**Figure 2 | Results from linear analysis and numerical simulations, showing the effect of stress exponent  $n$  on the angular dependence of porosity of melt bands.** **a**, The growth rate  $\dot{s}$  of porosity as a function of angle; equation (2). **b**, The normalized amplitude of melt-band porosity as a function of  $\theta$  and  $n$  for  $\gamma = 1$ . Advection by simple shear preferentially rotates higher-angle bands out of favourable orientation for growth. The angle with peak amplitude at a given strain is determined by the growth rate and the rate of passive rotation by simple shear. **c**, Normalized, binned amplitude of FFTs of the porosity field from an ensemble of numerical simulations with  $n = 6$  ( $n = 1, 4$  shown in Supplementary Fig. S4). Linear analysis is used to extend simulation results to

$\gamma = 3.6$  (Supplementary Fig. S2 shows angle evolution from linear analysis only). The colour scale goes from zero to one. **d**, Summary of simulation ensemble results for  $n = 1, 2, 4$  and 6. Coloured symbols represent the peak of the band-angle histogram and each is consistent with the angle estimated by visual inspection of the porosity field. Black symbols with 1-sigma error bars represent mean band angles in experiments, quantified by hand-measurement of sectioned experimental-run products. Black lines demonstrate the rotational effect of unperturbed simple shear on selected initial band angles (Supplementary equation S17). The behaviour of full nonlinear calculations for high strain at  $n > 3$  is still unclear.

angle have a larger amplitude than those at high angle. The systematics of band rotation are detailed in Supplementary equation S17.

The linear analysis suggests that increasing the contribution of strain-rate weakening favours the growth of low-angle melt bands. To validate these results and to explore the behaviour of the full non-linear system requires computational solutions, which we have performed using the Portable Extensible Toolkit for Scientific computation<sup>16,17</sup> (see Supplementary Information). The simulations are initiated at a constant porosity plus <1% random noise. Output from a representative run is shown in Fig. 1b and c.

Histograms of the distribution of band angles are calculated from simulations by taking the two-dimensional fast fourier transform (FFT) of the porosity field and integrating the amplitude response within 5° bins in band angle  $\theta$  (Fig. 1d). An ensemble of simulations is run, each with the same  $n$  but different initial noise, to produce a composite histogram at each time-step. Figure 2c shows the evolution of the band-angle distribution with increasing strain for  $n = 6$ . The peak of this histogram is initially  $\sim 15^\circ$  and persists at low angle with increasing strain. The evolution of the peak angle is also shown by magenta circles in Fig. 2d, which charts the peak angle for ensembles of simulations with different  $n$ . Consistent with the linear analysis, a more nonlinear viscosity (higher  $n$ ) results in a lower initial peak band angle.

In Fig. 2d, the angle corresponding to the peak of each of the histograms increases with strain for all  $n$ . Although the increase is due to the rotational effect of advection by simple shear, the rate of increase cannot be fully explained by this rotation. Black curves in Fig. 2c and d show the angle of material lines as they are advected by unperturbed simple shear flow. It is evident that the orientations of melt bands produced in simulations and linear analysis do not track with these trajectories. The trajectories that melt bands follow have a lower rate of increase in angle with strain than do the black curves. These trajectories result from an interplay of the growth of melt bands in favoured orientation and the rotation of bands out of this orientation by simple shear. An animation of calculations with  $n = 6$  (Supplementary movie M1) shows reconnection of porosity bands, maintaining the dominance of those at low angle. This reorganization is similar to the pumping mechanism proposed by Holtzman

*et al.*<sup>18</sup>, in which fluid flows from bands that have been rotated to higher angles to newly forming bands at lower angles.

Data from experiments are shown by black symbols in Fig. 2c and d and can be directly compared to model results. These data show that the peak band angle is roughly constant at  $15\text{--}20^\circ$  to large strain. Up to  $\gamma \approx 2$ , the data are consistent with simulations with  $n = 4$  or 6. Our current numerical techniques have not been able to take these simulations to higher strain (see Supplementary Information). Linear analysis, which tends to give higher peak band angles at a given strain than do simulations (see Fig. 2d), can be used to extend band-angle evolution to higher strain than that achieved in simulations (Fig. 2c). In this case, the results for  $n = 6$  are most consistent with the data. However, nonlinear effects in numerical simulations such as band reconnection and realignment might lead to a lower peak band angle at a given  $n$ .

The general agreement between our calculations and experimental results helps to validate magma dynamics theory. In particular, both theory and experiment exhibit the emergence of low-angle melt bands on length scales shorter than the compaction length that persist at low angle and concentrate shear strain. This agreement demonstrates the importance of non-newtonian rheology for modelling deforming, partially molten aggregates. In detail, there are differences between experiments and theory. For example, bands produced in simulations have a smaller aspect ratio and edges that are less sharp than those in experiments. These differences may result from the specific form of the flow law that we have used. More work is needed to explore models that use other non-newtonian rheologies and other formulations of magma dynamics<sup>8</sup>. Nevertheless, both experiments and theory suggest that deformation-induced melt bands are a robust feature of partially molten aggregates.

These results have implications for magma transport in the mantle, for example beneath mid-ocean ridges. A fundamental observation of mid-ocean ridges is that the oceanic crust is formed within 10 km of the ridge axis, whereas melt production is believed to occur over a region extending about 100 km from the axis<sup>19</sup>. This implies some mechanism of melt focusing toward the axis. The melt-band-forming instability may contribute to melt focusing, in addition to other mechanisms that have been proposed<sup>20–22</sup>. To estimate the orientation of bands, we calculate the principal axes of the strain-rate tensor for flow beneath a mid-ocean ridge<sup>23</sup> (Fig. 3a). Red line segments are perpendicular to the axis of maximum extension rate and show the orientation of melt bands expected for a newtonian viscosity, which tend to point away from the ridge axis. However, experiments (and theory for non-newtonian viscosity) suggest that band orientation is rotated  $25^\circ$  from the red line segments and should be most pronounced in regions of high strain. With these assumptions, melt bands point towards the ridge axis (Fig. 3b). If melt bands form an interconnected, permeable network with this orientation, they would enhance focusing of melt<sup>24</sup>. To quantitatively test this conjecture requires large-scale magma dynamics simulations ( $\sim 100$  km) that include the effects of melt buoyancy and finite strain, with sufficiently fine spatial discretization to resolve features smaller than the compaction length ( $\sim 1\text{--}10$  km)<sup>5,13</sup>. Such calculations will be challenging but current results give confidence that simulations can be used to predict patterns of melt extraction from the mantle.

Received 2 January; accepted 30 June 2006.

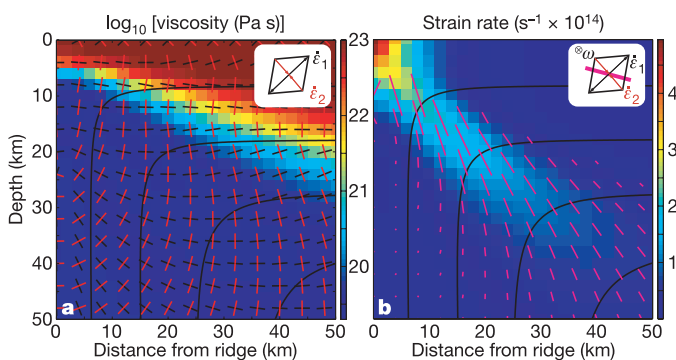


**Figure 3 | Estimated orientation of melt bands beneath a mid-ocean ridge from a two-dimensional, steady-state simulation of mantle flow<sup>23</sup>.** All fields have reflection symmetry about the line  $x = 0$ . **a**, Viscosity (colour), flow field (black streamlines), and principal axes of the strain-rate tensor for a temperature and strain-rate-dependent rheology. Red lines are perpendicular to the direction of maximum extension. For newtonian viscosity ( $n = 1$ ), red lines correspond to the orientation of melt bands in our model. Such bands would not focus melt toward the ridge axis. **b**, Strain rate (colour), flow field and melt-band orientation consistent with experiments (or in our model with  $n \approx 4\text{--}6$ ). Band orientations, indicated by magenta line segments, are calculated by rotating the red lines by  $25^\circ$  in the direction counter to the vorticity. The length of these segments is scaled to the local strain rate. If the bands form an interconnected permeable network, this orientation could help to focus melt to the ridge axis.

- Zimmerman, M., Zhang, S., Kohlstedt, D. & Karato, S. Melt distribution in mantle rocks deformed in shear. *Geophys. Res. Lett.* **26**, 1505–1508 (1999).
- Holtzman, B., Groebner, N., Zimmerman, M., Ginsberg, S. & Kohlstedt, D. Stress-driven melt segregation in partially molten rocks. *Geochem. Geophys. Geosyst.* **4**, 8607 (2003).
- Stevenson, D. Spontaneous small-scale melt segregation in partial melts undergoing deformation. *Geophys. Res. Lett.* **16**, 1067–1070 (1989).
- Spiegelman, M. Linear analysis of melt band formation by simple shear. *Geochem. Geophys. Geosyst.* **4**, 8615, doi:10.1029/2002GC000499 (2003).
- McKenzie, D. The generation and compaction of partially molten rock. *J. Petrol.* **25**, 713–765 (1984).

6. Scott, D. & Stevenson, D. Magma ascent by porous flow. *J. Geophys. Res.* **91**, 9283–9296 (1986).
7. Fowler, A. A mathematical model of magma transport in the asthenosphere. *Geophys. Astrophys. Fluid Dyn.* **33**, 63–96 (1985).
8. Bercovici, D., Ricard, Y. & Schubert, G. A two-phase model for compaction and damage 1. General theory. *J. Geophys. Res.* **106**, 8887–8906 (2001).
9. Hirth, G. & Kohlstedt, D. in *The Subduction Factory* (ed. Eiler, J.) 83–105 (AGU Geophysical Monograph 138, American Geophysical Union, Washington DC, 2003).
10. Richardson, C. Melt flow in a variable viscosity matrix. *Geophys. Res. Lett.* **25**, 1099–1102 (1998).
11. Hall, C. & Parmentier, E. Spontaneous melt localization in a deforming solid with viscosity variations due to water weakening. *Geophys. Res. Lett.* **27**, 9–12 (2000).
12. Karato, S. & Wu, P. Rheology of the upper mantle: A synthesis. *Science* **260**, 771–778 (1993).
13. Kelemen, P., Hirth, G., Shimizu, N., Spiegelman, M. & Dick, H. A review of melt migration processes in the adiabatically upwelling mantle beneath oceanic spreading ridges. *Phil. Trans. R. Soc. Lond. A* **355**, 283–318 (1997).
14. Mei, S., Bai, W., Hiraga, T. & Kohlstedt, D. Influence of melt on the creep behavior of olivine-basalt aggregates under hydrous conditions. *Earth Planet. Sci. Lett.* **201**, 491–507 (2002).
15. Kelemen, P., Shimizu, N. & Salters, V. Extraction of mid-ocean-ridge basalt from the upwelling mantle by focused flow of melt in dunite channels. *Nature* **375**, 747–753 (1995).
16. Knepley, M., Katz, R. & Smith, B. in *Numerical Solution of Partial Differential Equations on Parallel Computers* (eds Bruaset, A. & Tveito, A.) 413–438 (Lecture Notes in Computational Science and Engineering Vol. 51, Springer, Berlin, 2006).
17. Balay, S. *et al.* Portable Extensible Toolkit for Scientific computation (PETSc) (<http://www.mcs.anl.gov/petsc>) (2001).
18. Holtzman, B., Kohlstedt, D. & Morgan, J. P. Viscous energy dissipation and strain partitioning in partially molten rocks. *J. Petrol.* **46**, 2593–2613 (2005).
19. Forsyth, D. *et al.* Imaging the deep seismic structure beneath a mid-ocean ridge: the melt experiment. *Science* **280**, 1215–1218 (1998).
20. Spiegelman, M. & McKenzie, D. Simple 2-D models for melt extraction at mid-ocean ridges and island arcs. *Earth Planet. Sci. Lett.* **83**, 137–152 (1987).
21. Morgan, J. Melt migration beneath mid-ocean spreading centers. *Geophys. Res. Lett.* **14**, 1238–1241 (1987).
22. Sparks, D. & Parmentier, E. Melt extraction from the mantle beneath spreading centers. *Earth Planet. Sci. Lett.* **105**, 368–377 (1991).
23. Katz, R., Spiegelman, M. & Carbotte, S. Ridge migration, asthenospheric flow and the origin of magmatic segmentation in the global mid-ocean ridge system. *Geophys. Res. Lett.* **31**, L15605, doi:10.1029/2004GL020388 (2004).
24. Daines, M. & Kohlstedt, D. Influence of deformation on melt topology in peridotites. *J. Geophys. Res.* **102**, 10257–10271 (1997).

**Supplementary Information** is linked to the online version of the paper at [www.nature.com/nature](http://www.nature.com/nature).

**Acknowledgements** This work was supported by the Department of Energy Computational Science Graduate Fellowship Program of the Office of Science and National Nuclear Security Administration in the Department of Energy, and the NSF. We thank B. Smith, M. Knepley and the PETSc team at Argonne National Laboratory. We are also grateful to E. Coon, P. Kelemen and the solid Earth geodynamics group at LDEO for discussions. Comments by M. Jellinek helped to improve the manuscript.

**Author Information** Reprints and permissions information is available at [npg.nature.com/reprintsandpermissions](http://npg.nature.com/reprintsandpermissions). The authors declare no competing financial interests. Correspondence and requests for materials should be addressed to R.F.K. ([katz@ldeo.columbia.edu](mailto:katz@ldeo.columbia.edu)).

# The dynamics of melt and shear localization in partially molten aggregates

Richard F. Katz<sup>1</sup>, Marc Spiegelman<sup>1,2</sup> & Benjamin Holtzman<sup>1</sup>

<sup>1</sup>Lamont-Doherty Earth Observatory of Columbia University, Palisades, NY 10964

<sup>2</sup>Dept. of Applied Physics and Applied Math, Columbia University, New York, NY 10027

## Supplementary Information

A continuum theory of magma dynamics is applicable to the physical system considered here because both the system size ( $\sim 1$  mm) and the width of melt bands ( $\sim 100$   $\mu\text{m}$ ) are large compared to the grain size ( $\sim 10$   $\mu\text{m}$ ). Below we detail the derivation of equation (2) from the linearized magma dynamics equations of Spiegelman<sup>1</sup> (referred to as S03).

**Linearized non-Newtonian viscosity.** Past linear analysis considered a viscosity dependent only on porosity<sup>1</sup>. To extend this analysis to stress-dependent viscosity we linearize the relation between viscosity, porosity and strain rate

$$\eta(\phi, \mathbf{V}) = \eta_0 e^{\alpha(\phi-\phi_0)} \dot{\epsilon}_{II}^{\frac{1-n}{n}}. \quad (\text{S1})$$

We first expand the  $\phi$ -dependence in a Taylor series for  $\phi = \phi_0 + \varepsilon\phi_1$

$$e^{\alpha(\phi-\phi_0)} \approx 1 + \varepsilon\alpha\phi_1, \quad (\text{S2})$$

where  $\varepsilon$  is a number that is small compared with unity such that terms of order  $\varepsilon^2$  can be neglected.

We also need a linearized version of the second invariant of the strain rate tensor  $\dot{\epsilon}_{II} = \sqrt{\dot{\epsilon}_{ij}\dot{\epsilon}_{ij}}$ .

Following S03 the matrix velocity can be written as a background simple shear flow plus a small perturbation. The perturbation can be split into incompressible and volumetric flow components represented by a vector potential  $\psi_1$  and a scalar potential  $\mathcal{U}_1$ :

$$\mathbf{V} = \dot{\gamma}y\mathbf{i} + \varepsilon (\nabla \times \psi_1\mathbf{k} + \nabla\mathcal{U}_1) \quad (\text{S3})$$

Using equation (S3), the second invariant can be recast in terms of the velocity potentials

$$\dot{\epsilon}_{11} = \varepsilon \left( \frac{\partial^2\psi_1}{\partial x\partial y} + \frac{\partial^2\mathcal{U}_1}{\partial x^2} \right), \quad (\text{S4})$$

$$\dot{\epsilon}_{22} = \varepsilon \left( \frac{\partial^2\mathcal{U}_1}{\partial y^2} - \frac{\partial^2\psi_1}{\partial x\partial y} \right), \quad (\text{S5})$$

$$\dot{\epsilon}_{12} = \frac{1}{2} \left[ \dot{\gamma} + \varepsilon \left( 2\frac{\partial^2\mathcal{U}_1}{\partial x\partial y} + \frac{\partial^2\psi_1}{\partial y^2} - \frac{\partial^2\psi_1}{\partial x^2} \right) \right] \equiv \frac{1}{2} (\dot{\gamma} + \varepsilon\Psi). \quad (\text{S6})$$

It is important to note that  $\Psi$  contains contributions from both the incompressible and compressible components of the velocity field. It remains unclear whether the compressible component of velocity should contribute to weakening of the material. We have decided to include the compressible part for generality but describe below that for the ratio of bulk to shear viscosity in the experimentally estimated range<sup>2,3</sup> its effect is small. Using the velocity potentials, the strain rate dependence of viscosity can be written

$$\dot{\epsilon}_{II}^{\frac{1-n}{n}} \approx \left( \frac{\dot{\gamma}}{2} \right)^{\frac{1-n}{n}} \left( 1 + \varepsilon \frac{\Psi}{\dot{\gamma}} \right)^{\frac{1-n}{n}}. \quad (\text{S7})$$

We can apply Taylor expansion to the last term of equation (S7) to first order to give

$$\left( 1 + \varepsilon \frac{\Psi}{\dot{\gamma}} \right)^{\frac{1-n}{n}} \approx 1 + \varepsilon \frac{1-n}{n} \frac{\Psi}{\dot{\gamma}}. \quad (\text{S8})$$

Combining equations (S8), (S7) and (S1) gives the linearized viscosity

$$\eta(\phi_1, \mathbf{V}_1) \approx \eta_0 \left( 1 + \varepsilon \alpha \phi_1 + \varepsilon \frac{1-n}{n} \frac{\Psi}{\dot{\gamma}} \right), \quad (\text{S9})$$

where the constant  $\frac{\dot{\gamma}}{2} \frac{1-n}{n}$  has been absorbed into the viscosity pre-factor  $\eta_0$  and we have neglected  $O(\varepsilon^2)$  terms. From equation (S9) we can see that the first order perturbation to the background viscosity is given by

$$\eta_1(\phi_1, \mathbf{V}_1) = \eta_0 \left( \alpha \phi_1 + \frac{1-n}{n} \frac{\Psi}{\dot{\gamma}} \right). \quad (\text{S10})$$

**Linearized magma dynamics, scaling and a trial solution.** The dimensionless, linearized magma dynamics equations are<sup>1</sup>

$$\frac{\partial \phi_1}{\partial t} + y \frac{\partial \phi_1}{\partial x} = (1 - \phi_0) \mathcal{C}_1, \quad (\text{S11})$$

$$-\nabla^2 \mathcal{C}_1 + \mathcal{C}_1 = 2\xi \frac{\partial^2 \eta_1}{\partial x \partial y}, \quad (\text{S12})$$

$$\nabla^2 \mathcal{U}_1 = \mathcal{C}_1, \quad (\text{S13})$$

$$\nabla^4 \psi_1 = \frac{\partial^2 \eta_1}{\partial x^2} - \frac{\partial^2 \eta_1}{\partial y^2} \quad (\text{S14})$$

where  $\mathcal{C}_1$  is the dimensionless perturbation compaction rate,  $\mathcal{C}_1 = \nabla \cdot \mathbf{V}_1$ .  $\xi = \eta_0 / (\zeta_0 + 4\eta_0/3)$  where  $\zeta_0$  and  $\eta_0$  are the background bulk and shear viscosity, respectively. Because the ratio of bulk to shear viscosity  $\zeta_0/\eta_0$  must be positive,  $\xi$  is constrained to lie between 0 and  $\frac{3}{4}$ . Only the zeroth order bulk viscosity term  $\zeta_0$  appears in the linear analysis. For simplicity and due to a lack of experimental constraints, we consider  $\zeta$  a constant ranging from one to ten  $\eta_0^{2,3}$  in numerical simulations reported. Simulations where  $\zeta$  varies with porosity have been carried out and are indistinguishable from those with constant  $\zeta$ .

In equations (S11)-(S14) time is non-dimensionalized by the background strain rate such that  $t = \gamma$ , the total strain. Lengths are non-dimensionalized by the compaction length at porosity  $\phi = \phi_0$ , *i.e.*  $\delta = \sqrt{k_0(\zeta_0 + 4\eta_0/3)}/\mu$ . The compaction length is the intrinsic length scale that arises from the magma dynamics equations<sup>4</sup>. See paragraphs 8 and 10 in S03 for details. To complete the linear analysis we assume trial solutions  $\mathcal{C}_1 = \mathcal{C}^*(t)\phi_1$ ,  $\mathcal{U}_1 = \mathcal{U}^*(t)\phi_1$ ,  $\psi_1 = \psi^*(t)\phi_1$  where

$$\phi_1 = \exp [i\mathbf{k}(t) \cdot \mathbf{x} + s(t)] \quad (\text{S15})$$

and  $\mathcal{C}_1^*$ ,  $\psi_1^*$  and  $\mathcal{U}_1^*$  are scalar, possibly complex, functions of time only.  $\mathbf{k}(t)$  is the time-dependent wavevector

$$\mathbf{k}(t) = k_x \mathbf{i} + k_y(t) \mathbf{j} = k_x^0 \mathbf{i} + (k_y^0 - k_x^0 t) \mathbf{j} \quad (\text{S16})$$

where  $\mathbf{k}^0$  is the wavevector at  $t = 0$ . Equation (S16) gives the evolution of a wavefront evolving passively under advection by unperturbed simple shear flow (see S03 paragraph 13 for details).

The effect of advection by simple shear flow appears as a band rotation whose rate depends on angle. Equation (S16) can be recast to find the passively advected band angle as a function of time,

$$\theta(t) = \tan^{-1} \left[ \frac{\sin \theta_0}{\cos \theta_0 - t \sin \theta_0} \right], \quad (\text{S17})$$

where  $\theta_0 = \tan^{-1}[k_x^0/k_y^0]$  is the initial angle and  $t$  is dimensionless time. Passive advection trajectories for  $\theta(t)$  are shown as black lines in Figure 2c–d.

**Solutions to the linearized magma dynamics equations.** Given definitions for  $\phi_1$  and  $\Psi$ , we write the dimensionless, first order viscosity as

$$\eta_1(\mathbf{x}, t) = \left[ \alpha + \frac{1-n}{n} (k_x^2 \psi^* - k_y^2 \psi^* - 2k_x k_y \mathcal{U}^*) \right] \phi_1. \quad (\text{S18})$$

Substituting equations (S15), (S18) and the other trial solutions into equations (S11)-(S14) we obtain

$$\frac{ds}{dt} = (1 - \phi_0) \mathcal{C}^*, \quad (\text{S19})$$

$$\mathcal{C}^* = -2\xi \frac{k_x k_y}{k^2 + 1} \left[ \alpha + \frac{1-n}{n} (k_x^2 \psi^* - k_y^2 \psi^* - 2k_x k_y \mathcal{U}^*) \right], \quad (\text{S20})$$

$$\mathcal{U}^* = -\frac{\mathcal{C}^*}{k^2}, \quad (\text{S21})$$

$$\psi^* \left[ 1 + \frac{1-n}{n} \frac{(k_x^2 - k_y^2)^2}{k^4} \right] = -\frac{(k_x^2 - k_y^2)}{k^4} \left[ \alpha - 2k_x k_y \frac{1-n}{n} \mathcal{U}^* \right], \quad (\text{S22})$$

where  $k^2 = \mathbf{k} \cdot \mathbf{k}$ . Combining equations (S20)-(S22) and performing some algebra we arrive at

$$\mathcal{C}^* = -2\xi \alpha \frac{k_x k_y k^4}{(k^2 + 1) \left[ k^4 + \frac{1-n}{n} (k_x^2 - k_y^2)^2 \right] + 4 \frac{1-n}{n} \xi k_x^2 k_y^2 k^2}, \quad (\text{S23})$$

which, in the Newtonian limit ( $n = 1$ ), reduces to the solution obtained in S03,

$$\mathcal{C}^* = -2\xi \alpha \frac{k_x k_y}{k^2 + 1}. \quad (\text{S24})$$

Inspection of equation (S23) shows that for wavenumbers  $k^2 \ll 1$  (dimensionally, wavelengths much longer than the compaction length),  $\mathcal{C}^* \rightarrow 0$  approximately as  $k^2$ . This means that perturbations larger than the compaction length do not grow and we can concern ourselves with short wavelength perturbations where  $k^2 \gg 1$ . In this case we can rewrite equation (S23) as a function of perturbation band angle  $\theta$ :

$$\mathcal{C}^* = -\frac{\alpha \xi \sin(2\theta)}{1 + \frac{1-n}{n} [\cos^2(2\theta) + \xi \sin^2(2\theta)]} \quad (\text{S25})$$

by using the geometric relations  $k_x = |\mathbf{k}(t)| \sin \theta(t)$  and  $k_y = |\mathbf{k}(t)| \cos \theta(t)$  and trigonometric identities. Substituting equation (S25) into equation (S19) gives  $\dot{s}$ , which is shown in Figure 2a as a function of  $\theta$ . The velocity potential factors  $\psi^*$  and  $\mathcal{U}^*$  can similarly be expressed in terms of  $\theta$ . If we had chosen a form for the viscosity independent of compaction then the  $\sin^2(2\theta)$  term in the denominator of equation (S25) would not appear in this expression. This change has the effect of collapsing all four curves in Figure 2a to the same value at  $45^\circ$ .

Substituting equation (S23) into equation (S19) and integrating gives the natural log of the amplitude of the porosity perturbation as a function of strain,

$$s(\theta, \gamma) = - \int_0^\gamma \frac{\alpha \xi (1 - \phi_0) \sin(2\theta)}{1 + \frac{1-n}{n} [\cos^2(2\theta) + \xi \sin^2(2\theta)]} d\tau. \quad (\text{S26})$$

Figure 2b shows a plot of equation (S26) evaluated at a strain of  $\gamma = 1$  ( $t = 1$ ) for a range of angles,  $\theta$ . To show the evolution of porosity perturbation amplitude as a function of angle, Figure S2 shows a plot of equation (S26) evaluated at strains from one to four and angles of zero to  $90^\circ$ . These images should be compared to the results of numerical simulations such as those in Figure 2c.

At small strains  $\delta\gamma \ll 1$ , the log of the amplitude of porosity is approximately  $s(\theta, \delta\gamma) \approx \dot{s}\delta\gamma$  and the maxima of  $s(\theta, \delta\gamma)$  are the same as the maxima of  $\dot{s}$ . Taking the derivative of equation (2) with respect to  $\theta$ , setting to zero and solving gives three solutions for  $0 \leq \theta \leq 90$ . For  $n \leq (2 - \xi)/(1 - \xi)$ , only the solution  $\theta = \pi/4$  is real valued and represents the sole maximum at  $45^\circ$ . When  $n$  increases past this bound however, two other solutions become pure real and represent the

symmetric maxima of  $s$

$$\theta_{max} = \frac{1}{2} \arctan \left[ \pm (-2 + n + \xi - n\xi)^{-1/2} \right] \quad (\text{S27})$$

and the solution at  $45^\circ$  becomes a local minimum. This pattern, already evident in Figure 2a, is shown for a continuous range of  $n$  in Figure S3. The assumption that compaction contributes to viscosity variations means that different values of the ratio of bulk to shear viscosity correspond to different curves. The result without this assumption is indistinguishable from the black curve. Experiments<sup>2,3</sup> have roughly constrained the bulk viscosity to lie between 1 and 10 times the shear viscosity. Even if the bulk viscosity is within this range, for a given band angle (say  $20^\circ$ ) there is significant difference between the  $n$  required along the blue curve and the green curve in Figure S3. For the results of numerical simulations plotted in Figure 1, a value of  $\zeta_0/\eta_0 = 10$  has been assumed. If compaction strain does not contribute to determining the local shear viscosity there is little change in the preferred value of  $n$ . If, however, compaction strain is important and the ratio of bulk to shear viscosity is on the low end of expected values,  $\zeta_0/\eta_0 \approx 1$ , then linear analysis would predict that a higher  $n$  is needed to make simulations consistent with data (see Figure 2d for a comparison). This is an important point to resolve in future work because it affects both the value of  $n$  preferred by our model as well as the behavior of the magma/mantle dynamics system in other contexts (such as reactive melting calculations<sup>5</sup>).

The amount of strain over which the linear analysis remains valid depends partly on  $\alpha\xi$ . For typical parameter values, predictions of amplitude break down by strains of  $\gamma \lesssim 1$ . However, a comparison to numerical solutions suggests that predictions of angular distributions are surprisingly good to large strains.

**Numerical simulations.** The simulations described above and shown in Figure 1b and c represent numerical solutions of the magma dynamics equations<sup>4</sup>

$$\frac{\partial \phi}{\partial t} + \mathbf{V} \cdot \nabla \phi = (1 - \phi) \nabla \cdot \mathbf{V}, \quad (\text{S28})$$

$$\nabla \cdot \mathbf{V} = \nabla \cdot \frac{k_\phi}{\mu} \nabla P, \quad (\text{S29})$$

$$\nabla P = \nabla \cdot [\eta (\nabla \mathbf{V} + \nabla \mathbf{V}^T)] + \nabla \cdot \left[ \left( \zeta - \frac{2\eta}{3} \right) \nabla \cdot \mathbf{V} \right], \quad (\text{S30})$$

where  $\phi$  is porosity,  $\mathbf{V}$  is solid velocity,  $P$  is the dynamic pressure,  $k_\phi$  is permeability ( $k_\phi \propto \phi^n$ ),  $\mu$  is the melt viscosity,  $\eta$  is the shear viscosity of the solid and  $\zeta$  is the bulk viscosity of the solid. Terms representing the buoyancy force and mass transfer between solid and fluid are not included because they are negligible in the experiments. The equations are discretized using a semi-implicit finite volume scheme on a staggered mesh. The domain is periodic in the horizontal. On the top and bottom boundaries the matrix velocity is required to satisfy  $\mathbf{V} = \pm U_0 \mathbf{i} + 0 \mathbf{j}$  and vertical gradients in pressure and porosity are required to equal zero. The resulting system of discrete non-linear equations is solved within the Portable Extensible Toolkit for Scientific computing (PETSc) framework using a Newton-Krylov-Schwartz method with GMRES and an incomplete LU factorization preconditioner<sup>6,7</sup>. The simulations were run until they failed to converge, which typically occurred when inter-band porosity reached zero or when localization resulted in very sharp gradients in material properties.

To investigate the effect of varying the stress-dependence of viscosity we ran 4 groups of simulations at  $n = 1, 2, 4, 6$ . Each group consisted of 4 model runs at different grid resolutions from 50 to 80 cells per compaction length on a domain of 4x2 compaction lengths. Each run was

initiated with 5 vol% background porosity with 0.05 vol% white noise perturbation (the power spectrum of the initial noise field controls the wavelength of the emergent band pattern but does not affect the angle distribution). In these simulations we specified a constant bulk viscosity. In other simulations we have relaxed this assumption and allowed bulk viscosity to vary either with porosity or as a multiple of the shear viscosity. In both cases, results were qualitatively identical to the constant bulk viscosity case.

To quantify the distribution of band angles, a FFT was applied to the porosity field at each time-step and the resulting amplitude spectrum was binned by angle. The histograms for each group at each time-step were then summed and normalized to give plots of histogram amplitude as a function of strain and band angle. Figure 2c shows the result for  $n = 6$ ; for  $n = 1$  and 4 see Figure S4. In contrast to linear analysis results (Figure S3), simulations do not produce high-angle bands, even at small strains. Evidently increasing  $n$  in the simulations results in lower initial band angles and a narrower distribution of amplitude with angle.

An important question raised by the analysis of experiments and considered in the discussion of this paper regards the mechanism by which bands are maintained at low angle over large strains. Large strains would be expected to rotate initially low angle bands to high angles, according to equations (S17). S03 suggests one mechanism for maintaining low angle in which bands act as strain guides for matrix shear. These strain guides are assumed to modify the solid flow field significantly from simple shear, reducing the amount of rotation. Strain concentrations are observed in experiments<sup>8</sup> and in simulations (Figure 1b–c) where strain markers are offset across porosity bands. However, comparison of strain markers to their positions predicted by simple shear

in Figure 1b–c shows that the deviation from simple shear is small.

1. Spiegelman, M. Linear analysis of melt band formation by simple shear. *Geochem. Geophys. Geosyst.* **4** (2003). Article 8615, doi:10.1029/2002GC000499.
2. Cooper, R. Differential stress induced melt migration: an experimental approach. *J. Geophys. Res.* **95**, 6979–6992 (1990).
3. Renner, J., Visckupic, K., Hirth, G. & Evans, B. Melt extraction from partially molten peridotites. *Geochem. Geophys. Geosyst.* **4** (2003). 8606, doi:10.1029/2002GC000369.
4. McKenzie, D. The generation and compaction of partially molten rock. *J. Petrol.* **25**, 713–765 (1984).
5. Spiegelman, M., Kelemen, P. & Aharonov, E. Causes and consequences of flow organization during melt transport: the reaction infiltration instability in compactible media. *J. Geophys. Res.* **106**, 2061–2077 (2001).
6. Knepley, M., Katz, R. & Smith, B. Developing a geodynamics simulator with PETSc. In Bruaset, A. & Tveito, A. (eds.) *Numerical Solution of Partial Differential Equations on Parallel Computers*, vol. 51 of *Lecture Notes in Computational Science and Engineering* (Springer-Verlag, 2006).
7. Balay, S. *et al.* PETSc home page (2001). [Http://www.mcs.anl.gov/petsc](http://www.mcs.anl.gov/petsc).
8. Holtzman, B., Groebner, N., Zimmerman, M., Ginsberg, S. & Kohlstedt, D. Stress-driven melt segregation in partially molten rocks. *Geochem. Geophys. Geosyst.* **4** (2003). Art. No. 8607.

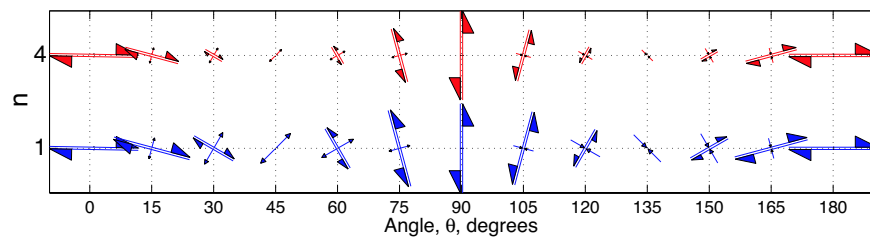


**Figure S1** This figure shows the relative sizes of the shear and volumetric components of the perturbation flow field for  $n = 1$  and 4. The velocities for  $n = 4$  are four times greater than those for  $n = 1$  but are scaled down to fit on the graph. It is evident from this panel that, independent of  $n$ , the volumetric component of strain goes to zero at  $0^\circ$  and  $90^\circ$  while the shear component goes to zero at  $45^\circ$  and  $135^\circ$ . Melt bands grow (de-compact) when oriented at angles less than  $90^\circ$  and decay (compact) when oriented at angles greater than  $90^\circ$ . The shear component is maximized at  $0^\circ$  and  $90^\circ$  to the shear plane.

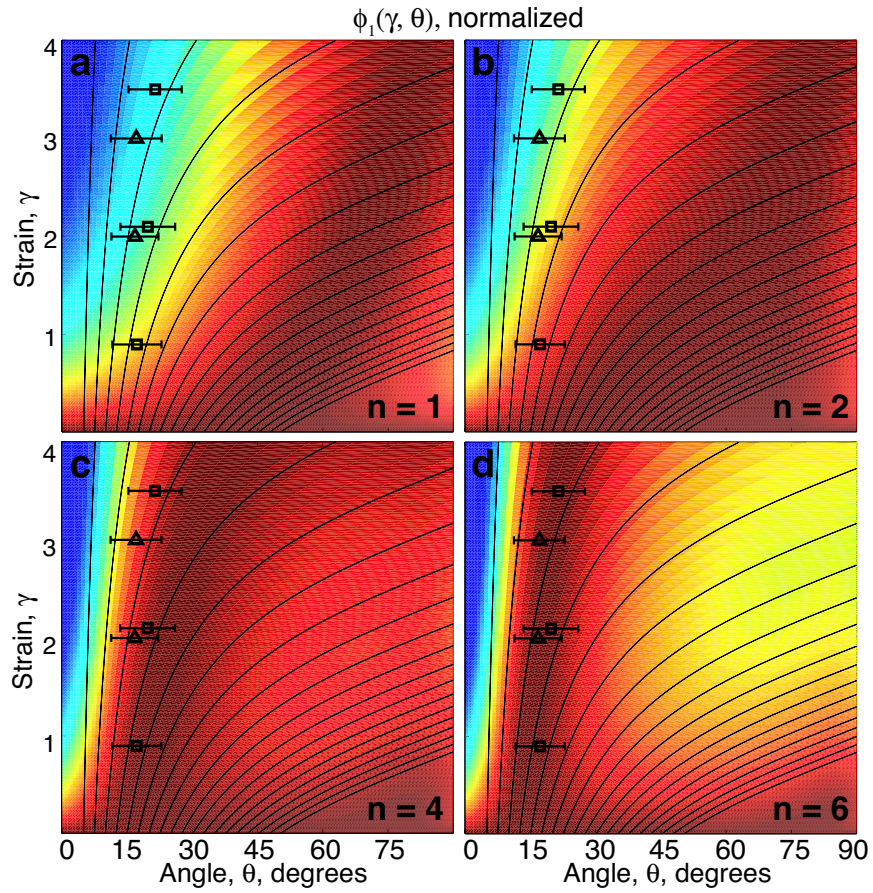


**Figure S2** Results from linear analysis showing the effect of stress exponent  $n$  on the distribution of melt band amplitude with angle, and its evolution with time (for bands with wavelengths shorter than the compaction length). Each figure is computed by integrating equation (S26) for an array of initial angles and final strains and then normalizing the angular distribution by its maximum value. The  $\sin^2(2\theta)$  term in the denominator, resulting from the contribution of compaction strain to viscosity, has been neglected in the calculations shown in these images. Data is as in Figure 2c–d.

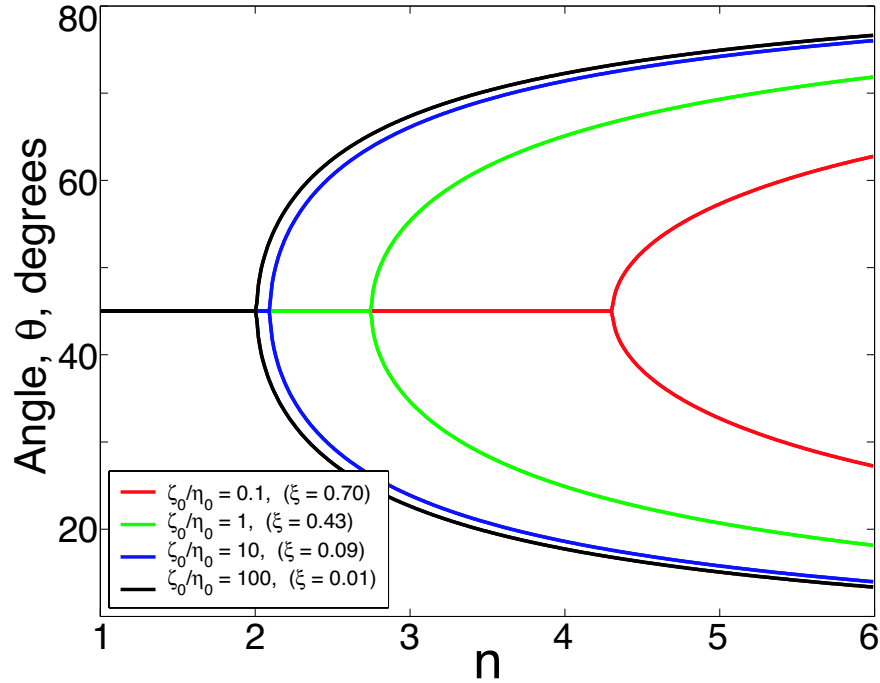


**Figure S3** The position of the maxima of  $\dot{s}$  as a function of  $n$ . Curves are obtained by plotting equation (S27) for different ratios of the bulk to shear viscosity  $\zeta_0/\eta_0$ . Neglecting the effect of compaction on viscosity gives a result indistinguishable from the black curve. These curves predict the angles at which melt bands will have the highest instantaneous porosity growth rate. To undergo significant accumulated growth, a band must remain near one of these favored angles. High angle bands represented by the upper branch of the curves in this figure are rapidly advected away from the angle of peak instantaneous growth to angles near and above  $90^\circ$  where they cease to grow and begin to compact. Low angle bands represented by the lower branch are not rotated strongly by advection (see advection trajectories due to unperturbed simple shear in Figure 2c, for example) and thus remain longer in a favorable position for growth of porosity. The amplitude  $e^{s(t)}$  of low angle bands thus increases faster than the amplitude of high angle bands.

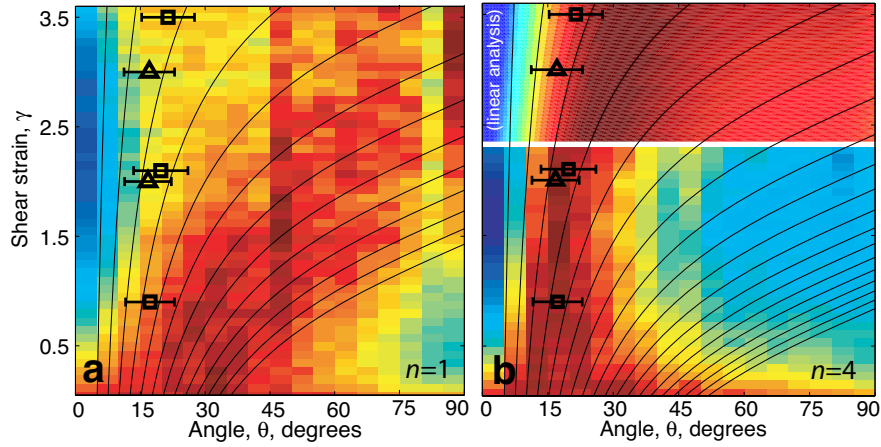


**Figure S4** Additional results from numerical simulations, as in Figure 2c but for  $n = 1$  and  $n = 4$ . Data and black lines are as described in the caption of Figure 2.

**Movie M1** An animation of simulation results from a run with  $\alpha = -27$  and  $n = 6$ . The bottom-left panel shows perturbation vorticity,  $\nabla \times [\mathbf{V} - \dot{\gamma}y\mathbf{i}]/\dot{\gamma}$ , the top-left panel shows the porosity field (volume fraction of fluid), and the panel at right shows the evolving band angle distribution from a 2D FFT of the porosity field binned by angle. Noise in the initial porosity field has a non-white spectrum: some high frequencies have been isotropically filtered to give the field short-wavelength spatial correlations. This is visible in the porosity field of the first frame of the movie and has the effect of increasing band width and spacing relative to runs with white noise perturbations to the initial porosity. Black solid lines and white dotted lines are advection tracers as in Figure 1b–c.